Redox-controlled conductance of polyoxometalate molecular junctions.

Cécile Huez,[1] David Guérin,[1] Stéphane Lenfant,[1] Florence Volatron,[2] Michel Calame,[3,4] Mickael L. Perrin,[3,5] Anna Proust[2] and Dominique Vuillaume.[1]

1) Institute for Electronics Microelectronics and Nanotechnology (IEMN), CNRS, University of Lille, Av. Poincaré, Villeneuve d'Ascq, France .

2) Institut Parisien de Chimie Moléculaire (IPCM), CNRS, Sorbonne Université, 4 Place Jussieu, F-75005 Paris, France.

3) EMPA, Transport at the Nanoscale Laboratory, 8600 Dübendorf, Switzerland.

4) Dept. of Physics and Swiss Nanoscience Institute, University of Basel, Klingelbergstrasse 82, 4056 Basel, Switzerland.

5) Department of Information Technology and Electrical Engineering, ETH Zurich, 8092 Zurich, Switzerland.

Abstract.

We demonstrate the reversible *in situ* photoreduction of molecular junctions of phosphomolybdate $[PMo_{12}O_{40}]^{3-}$ monolayer self-assembled on flat gold electrodes, connected by the tip of a conductive atomic force microscope. The conductance of the one electron reduced $[PMo_{12}O_{40}]^{4-}$ molecular junction is increased by ~ 10, this open-shell state is stable in the junction in air at room temperature. The analysis of a large current-voltage dataset by unsupervised machine learning and clustering algorithms reveals that the electron transport in the pristine phosphomolybdate junctions leads to symmetric current-voltage curves, controlled by the lowest unoccupied molecular orbital (LUMO) at 0.6-0.7

eV above the Fermi energy with ~25% of the junctions having a better electronic coupling to the electrodes than the main part of the dataset. This analysis also shows that a small fraction (~ 18% of the dataset) of the molecules is already reduced. The UV light *in situ* photoreduced phosphomolybdate junctions are systematically featuring slightly asymmetric current-voltage behaviors, which is ascribed to electron transport mediated by the single occupied molecular orbital (SOMO) nearly at resonance with the Fermi energy of the electrode and by a closely located single unoccupied molecular orbital (SUMO) at ~0.3 eV above the SOMO with a weak electronic coupling to the electrodes (~ 50% of the dataset) or at ~0.4 eV but with a better electrode coupling (~ 50% of the dataset). These results shed lights to the electronic properties of reversible switchable redox polyoxometalates, a key point for potential applications in nanoelectronic devices.

Keywords: polyoxometalate, redox, electron transport, molecular electronics, conductive AFM, machine learning.
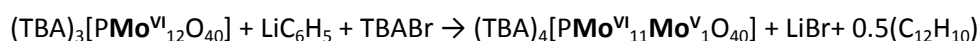
Introduction.

A reliable knowledge of the relationship between the redox state of polyoxometalates (POMs) and their electron transport (ET) properties, e.g., electrical conductance, at the nanoscale is mandatory for potential applications in POM-based nanoelectronic devices. At the material level (macroscopic scale), an increase by a factor of about 500 in the conductivity of a single crystal of $HK_{3,5}Li_{1,5}Co_4[NaP_5W_{30}O_{110}]$ was reported upon ultraviolet photoreduction.[1] However, at the device level, the redox state of the POMs is determined and tuned with the POMs embedded in a dielectric (insulating) layer (gate dielectric of a transistor,[2] stacked layer of a capacitance[3-6]). In this case, the direct relationship between the redox state of the POMs and their electrical conductance cannot be studied. At the nanoscale, monolayers (or few monolayers) of POMs assembled on conducting surfaces by various approaches (covalent grafting, electrostatically immobilization, layer-by-layer deposition,…) and contacted by scanning probe microscopy have been used to measure the conductance of various POMs,[7-12] but the redox state was not systematically tuned and controlled. It is only recently that at the single molecule level, using scanning tunneling microscopy, Linnenberg et al. demonstrated a step-by-step increase of the POM (Lindqvist-type V_6) conductance up to the 4-electron reduced state.[13, 14]

Here, we study by conductive atomic force microscopy (C-AFM) the ET of a monolayer of an "archetype" Keggin-type POM ($[PMo_{12}O_{40}]^{3-}$) assembled on Au surfaces. We demonstrate that the redox switching of the POMs in the monolayer is triggered *in situ* by UV photoreduction and is reversible upon dark condition at room temperature (or moderate heating) and we report an increase of the POM conductance by a factor ≈ 10 upon a one-electron reduction. This conductance switching is ascribed to a transition from a LUMO-mediated ET for the pristine (fully oxidized) $PMo_{12}(0)$ to a SOMO- and SUMO-mediated ET for the one-electron

reduced $PMo_{12}(I)$. The analysis of a large dataset (600 I-Vs measured by C-AFM) of the ET properties using unsupervised machine learning and clustering algorithms reveal that all the POM molecular junctions with the $PMo_{12}(0)$ display almost symmetric I-Vs, with nearly the same energy of the LUMO at around 0.6 - 0.7 eV above the Fermi energy of the electrodes and that about 25% of the molecular junctions have a better electronic coupling to the electrodes than the main part of the junctions in this dataset. The molecular junctions with the one-electron reduced $PMo_{12}(I)$ systematically display slightly asymmetric I-Vs (more current at a negative voltage applied on the Au substrate). The dataset is composed of two types of molecular junctions: one with the SUMO level at around 0.3 eV above the electrode Fermi level but with a weak electronic coupling to the electrodes (about half of the dataset), and the another one with the SUMO at about 0.4 eV but with a better electronic coupling to the electrodes. These features explain the large overall dispersion of the measured I-V dataset.

Synthesis of molecules and self-assembled monolayers, physico-chemical characterizations.

The fully oxidized (pristine) phosphomolybdate $[PMo_{12}O_{40}]^{3-}$ has been prepared as a tetrabutylammonium ($N(C_4H_9)_4^+$ or TBA^+) salt as reported in the literature.[15] Some of us have previously described its mono-electronic reduction by reaction with phenyllithium, according to the following equation.[16]

$$(TBA)_3[PMo^{VI}_{12}O_{40}] + LiC_6H_5 + TBABr \rightarrow (TBA)_4[PMo^{VI}_{11}Mo^{V}_{1}O_{40}] + LiBr + 0.5(C_{12}H_{10})$$

$(TBA)_3[PMo^{VI}_{12}O_{40}]$ ($PMo_{12}(0)$ for short) and $(TBA)_4[PMo^{VI}_{11}Mo^{V}_{1}O_{40}]$ ($PMo_{12}(I)$ for short) are thus available as yellow and blue powders, respectively. Relevant details about the characterization of the products (^{31}P NMR, cyclic voltammetry, solution

UV-vis spectra, XPS spectra on powder) are given in the Supporting Information (section 1). In particular, the cyclic voltammogram (Fig. S3),the UV-vis spectra of the POMs in solution (Fig. S4) and the XPS on powder (Mo $3d_{3/2}$ and $3d_{5/2}$ orbit doublet, Fig. S5) clearly show the reduction of the POMs.

For the monolayer preparation, we used ultra-flat template-stripped gold surface ^{TS}Au.[17] The freshly prepared ^{TS}Au surfaces were first functionalized with a 6-aminohexane-1-thiol hydrochloride (HS-$(CH_2)_6$-NH_3^+ / Cl^-) SAM (self-assembled monolayer), C6 SAM for short. Then these SAMs were treated by a PBS (phosphate-buffered saline, pH=7.4) solution for 2 hours, followed by ultra-sonication in DI water for 5 minutes to adjust the ratio of NH_3^+/NH_2 on the surface and optimize the next step (electrostatic deposition of the POMs) as reported in our previous work.[11] After this process, we estimate that ∼ 30% - 50% of the amine terminal groups are protonated (NH_3^+)-(details in the Supporting Information).[18-21] Then, the $PMo_{12}(0)$ and $PMo_{12}(I)$ molecules were electrostatically attached on these positively charged C6-SAMs by dipping the modified substrate in the POM solution (1h at 10^{-3}M in acetonitrile) and rinsed in acetonitrile, more details in the Supporting Information (section 2). The electrical neutrality is thus ensured by a mixture of the TBA^+ counterions and the NH_3^+ end-goups of the alkyl chains (see details in the Supporting Information).

The thickness of the SAMs was characterized by spectroscopic ellipsometry (see section 3 in the Supporting Information) at each step: 1.0 ± 0.2 nm for C6-SAM, 1.8 ± 0.2 nm for C6/$PMo_{12}(0)$ and C6/$PMo_{12}(I)$ SAMs. Tapping mode AFM images (Fig. 1) show that the C6-SAMs are flat with a rms roughness of ≈ 0.65 nm (reference for ^{TS}Au : 0.3-0.4 nm) and free of defects (no pinhole, nor aggregate, the dark spots are defects (pinhole) in the underlying Au substrate and they are

masked for the roughness analysis). After the deposition of the POMs, the surface is still featureless with a rms roughness of ≈ 0.56 nm for $PMo_{12}(0)$ and ≈ 0.73 nm for $PMo_{12}(I)$. These results indicate that the C6-SAMs are densely packed (the theoretical thickness for a fully packed SAM with the C6 alkyl chains almost perpendicular to the substrate is *ca.* 1.2 nm). The average thickness for the POM part is 0.8 nm, slightly smaller than the nominal size of the POM (1 nm), which can be explained considering the voids in a close-packed monolayer of spheres.[22] We conclude that the POM coverage is almost complete.
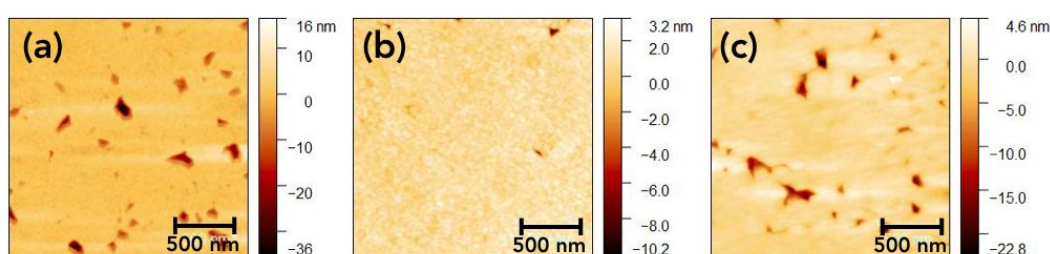

Figure 1. *Tapping-Mode AFM images of (a) ^{TS}Au-C6 SAM, (b) ^{TS}Au-C6/$PMo_{12}(0)$ and (c) ^{TS}Au-C6/$PMo_{12}(I)$. The dark spots are defects (pinhole) in the underlying Au substrate and they are masked for the roughness analysis. The rms roughness is 0.65 nm, 0.56 and 0.73 nm for the ^{TS}Au-C6 SAM, ^{TS}Au-C6/$PMo_{12}(0)$ and ^{TS}Au-C6/$PMo_{12}(I)$ samples, respectively.*

Electron transport properties.

The electron transport properties were measured by C-AFM for the two systems ^{TS}Au-C6/$PMo_{12}(0)$//Pt and ^{TS}Au-C6/$PMo_{12}(I)$//Pt ("-" denotes a chemical bond, "/" an electrostatic contact and "//" a mechanical contact). Typically up to 600 current-voltage (I-V) curves were acquired at several locations on the SAMs using

a C-AFM tip (Pt tip, grounded), at a low loading force F ≈ 6-8 nN (see details section 4 in the Supporting Information). Figure 2 shows the 2D histograms (heat map) of hundreds of I-V traces for both the ^{TS}Au-C6/PMo$_{12}$(0)//Pt and ^{TS}Au-C6/PMo$_{12}$(I)//Pt junctions prepared directly with the pristine and reduced POMs. In these datasets, we removed the I-V traces reaching the saturating current of the preamplifier during the voltage scan (typically ~3-7% IVs of the dataset) and those close to the sensitivity limit of the C-AFM (very noisy) or with large and abrupt changes in the measured current (C-AFM tip contact issue), typically ~15-20% of the IVs (see section 4 in the Supporting Information (Fig. S4) and the machine learning/clustering analysis below and in section 7 in the Supporting Information). For the ^{TS}Au-C6/PMo$_{12}$(0)//Pt sample a large number of I-V traces are low (<10^{-11} A) and noisy compared to the ^{TS}Au-C6/PMo$_{12}$(I)//Pt junction, which explains the smaller number of traces retained in the 2D histogram of the ^{TS}Au-C6/PMo$_{12}$(0)//Pt sample. The black lines in Figs. 2a and 2b are the calculated mean current I-V curve (denoted as Ī-V). The current histograms at + 1.5 V and -1.5 V are also shown in Figs. 2c and 2d, they are fitted by a log-normal distribution. The fitted parameters, the log-mean current (log-μ), the corresponding mean current Ī, and the log-standard deviation (log-σ) are summarized in Table 1. From these data, we clearly observe a larger increase of the current by a factor ≈ 10 for the PMo$_{12}$(I) molecules. We also observe a slight asymmetry of the I-Vs for the ^{TS}Au-C6/PMo$_{12}$(I)//Pt, with a negative asymmetry ratio R$^-$ = Ī(-1.5 V)/Ī(+1.5 V) ≈ 5.5 (evaluated from the mean of current histograms, Figs. 2c and 2d).

		^{TS}Au-C6/PMo$_{12}$(0)//Pt	^{TS}Au-C6/PMo$_{12}$(I)//Pt
+1.5V	**log-μ**	-9.92	-9.50
	Ī (A)	1.2×10^{-10}	3.1×10^{-10}
	log-σ	0.68	0.72
-1.5V	**log-μ**	-9.70	-8.80
	|Ī| (A)	2.0×10^{-10}	1.6×10^{-9}
	log-σ	0.43	0.36

Table 1. *Parameters of the log-normal fits of the current distributions at 1.5V and -1.5V (Figs. 2c and 2d): log-mean current (log-μ), the corresponding mean current Ī, and the log-standard deviation (log-σ).*
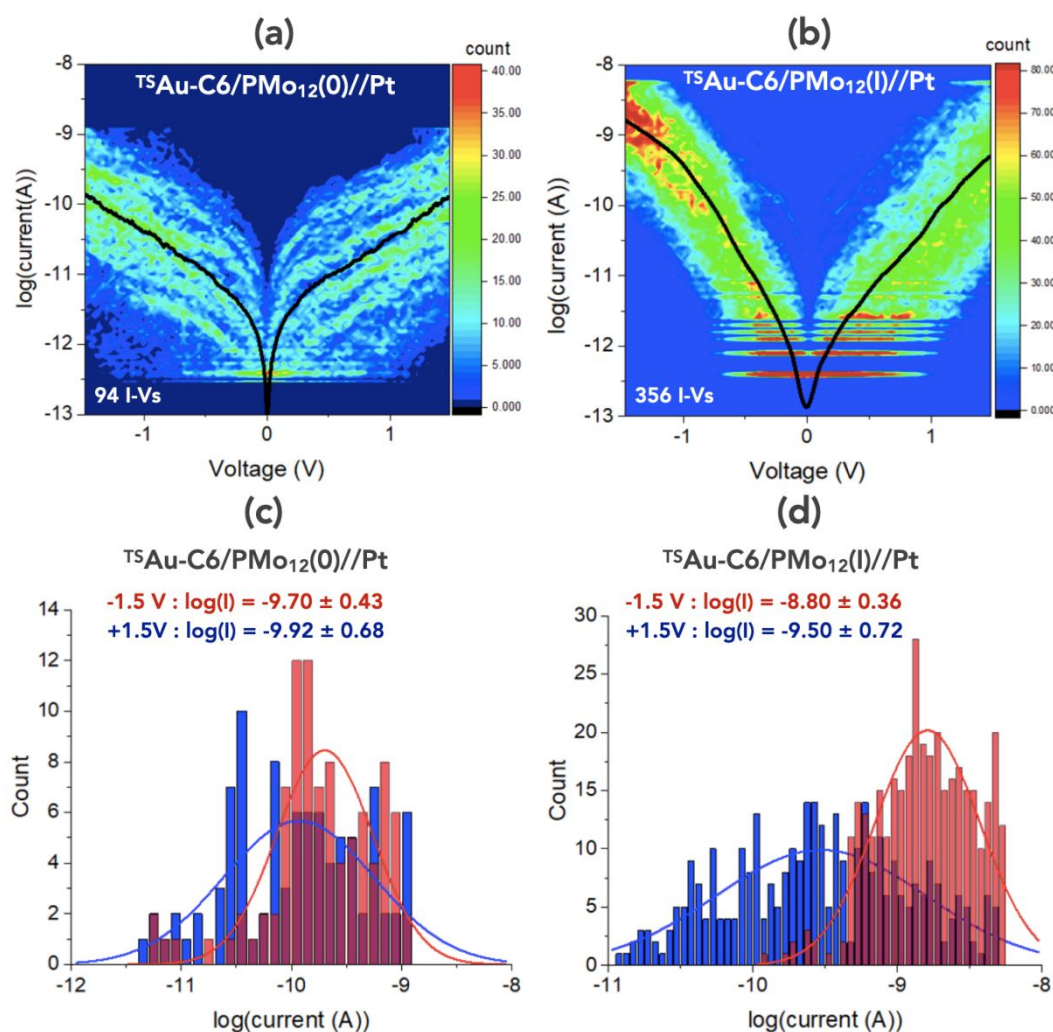
Figure 2. *2D histograms (heat maps) of I-Vs in a semi-log$_{10}$ plot for (a) ^{TS}Au-C6/PMo$_{12}$(0)//Pt and (b) ^{TS}Au-C6/PMo$_{12}$(I)//Pt. The solid black lines are the mean Ī-V curves. The histograms of the currents at -1.5 V (red bars) and +1.5V (blue bars) and fits by a log-normal distribution (the fitted log-mean value ± log-standard deviation is indicated on the panels).*

We then follow *in situ* by C-AFM the reversible reduction/re-oxidation of the POMs in the SAMs. Starting from a ^{TS}Au-C6/PMo$_{12}$(0)//Pt junction, we irradiate the POM layer with UV light (at 308 nm during few hours, see details sections 5 and 6 in the Supporting Information) and then we turn off the light and let the POM layer in ambient air either at room temperature (few tens of hours) or under a moderate heating (2h at 80°C on a hotplate in air). Both the POMs and the C6 SAMs are stable at this temperature (see in the Supporting Information). The I-Vs are measured after each step and the figure 3 shows the evolution the mean current (at -1 V) for 3 irradiation/relaxation cycles (Fig. S10 with more data). The complete dataset measured after each step is given in Fig. S10. A clear increase in the conductance is observed upon UV irradiation, followed by a return to a state of lower conductance after turning the light off. We note that the reduced state of the POMs in the junctions is stable long enough to do the C-AFM measurements (couple of hours) and that the return to the oxidized state laps for tens hours to a day (in air and at room temperature). From the experimental behavior of the monolayers directly prepared with the POMs in their PMo$_{12}$(0) and PMo$_{12}$(I) states described just above (Fig. 2), we can infer that the PMo12(0) monolayer is *in situ* photo-reduced and subsequently air re-oxidized. This is consistent with the reported photochemical reduction of polyoxometalates underlining their application in photochromic materials.[23] Irradiation in the UV range indeed results in oxygen-to-metal charge transfer transitions. This behavior was also checked on a drop cast film of PMo$_{12}$(0) on a glass substrate and irradiated with the same UV source (color change - see Fig. S11). We thus demonstrate that we are able to switch the redox state of the PMo$_{12}$ at the monolayer scale.
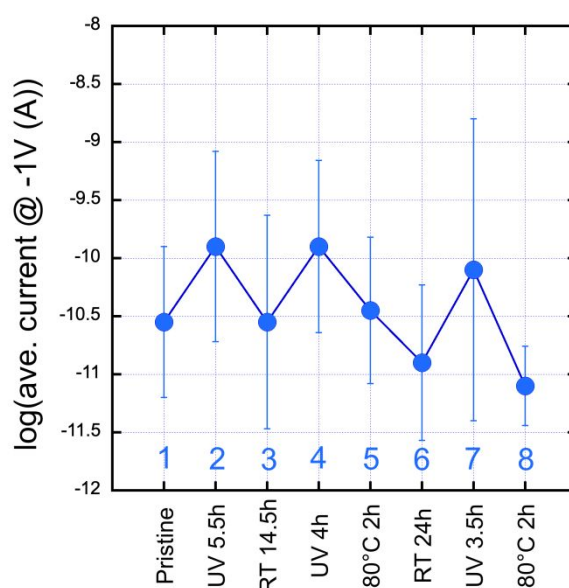
Figure 3. *Evolution of the mean current $log(|\bar{I}|)$ at -1V for 3 cycles of reduction/oxidation. The currents measured during the last cycle are lower, possibly due to some degradation of the sample or the tip or a drift of the C-AFM loading force (see the Supporting Information).*

To analyze the electronic structure in more detail, we fit all the individuals I-V curve in the dataset shown in Fig. 2 with the single-energy level (SEL) model (Eq. 1), considering that: i) a single molecular orbital (MO) dominates the charge transport, ii) the voltage mainly drops at the molecule/electrode interface and iii) that the MO broadening is described by a Lorentzian or Breit-Wigner distribution:[24, 25]

$$I(V) = N\frac{8e}{h}\frac{\Gamma_1\Gamma_2}{\Gamma_1+\Gamma_2}\left[\arctan\left(\frac{\varepsilon_{0-SEL}+\frac{\Gamma_1}{\Gamma_1+\Gamma_2}eV}{\Gamma_1+\Gamma_2}\right)-\arctan\left(\frac{\varepsilon_{0-SEL}-\frac{\Gamma_2}{\Gamma_1+\Gamma_2}eV}{\Gamma_1+\Gamma_2}\right)\right]$$

(1)

with $\varepsilon_{0\text{-SEL}}$ the energy of the MO involved in the transport (with respect to the Fermi energy of the electrodes), Γ_1 and Γ_2 the electronic coupling energy between the MO and the electron clouds in the two electrodes, e the elementary electron charge, h the Planck constant and N the number of molecules contributing to the ET in the molecular junction (assuming independent molecules conducting in parallel, *i.e.* no intermolecular interaction[26-28]). Albeit this number can be estimated using mechanical models of the tip/SAM interface in some cases when the Young modulus of the SAM is reasonably known,[29-33] this is not the case here for the POM/alkyl SAM system for which the Young modulus has not been determined. Consequently, we use N=1 throughout this work. This means that the Γ_1 and Γ_2 values are "effective" coupling energies of the SAM with the electrodes and they are used only for a relative comparison of the POM SAMs measured with the same C-AFM conditions in the present work and they cannot be used for a direct comparison with other reported data (as for example from single molecule experiment). We also note that the exact value of N has no significant influence on the fitted parameter ε_0. We also used the transition voltage spectroscopy (TVS)[34-38] to analyze the I-V curves. Plotting $|V^2/I|$ vs. V (Fig. S7),[39] we determine the transition voltages V_{T+} and V_{T-} for both voltage polarities at which the bell-shaped curve is maximum. This threshold voltage indicates the transition between off-resonant (below V_T) and resonant (above V_T) transport regime in the molecular junctions and can therefore be used to estimate the location of the energy level. The value of $\varepsilon_{0\text{-TVS}}$ is estimated by:[36]

$$\left|\varepsilon_{0-TVS}\right| = 2\frac{e\left|V_{T+}V_{T-}\right|}{\sqrt{V_{T+}^2 + 10\left|V_{T+}V_{T-}\right|\Big/3 + V_{T-}^2}}$$

(2)

We also determined an average value of the electrode coupling energy Γ_{TVS} using this relationship:[40, 41]

$$G(0) = NG_0 \frac{\Gamma^2_{TVS}}{\varepsilon^2_{0-TVS}}$$

(3)

with G(0) the zero-bias conductance, G_0 the conductance quantum ($2e^2/h = 7.75 \times 10^{-5}$ S, e the electron charge, h the Planck constant) and N the number of molecules in the junction. G is calculated from the slope of the I-V curve in its ohmic region (-50 mV/50 mV) and N=1 (see above). Note that Γ_{TVS} is equivalent to the geometrical average of the SEL values $(\Gamma_1\Gamma_2)^{1/2}$.[40, 41]

We combined the fit of the SEL model with the TVS method and we limited the fits of the SEL model to a voltage window -1 V to 1 V to obtain the best determination of ε_0 (see in the Supporting Information, section 4, for details on the fit protocol, Fig. S8). Also note that the SEL model is valid as long as the applied voltage does not drive the MO near the Fermi energy of the electrodes (*i.e.*, ET in the off-resonance situation), which is not the case for the $PMo_{12}(I)$. Consequently, this model is not used in that case (see section 4 in the Supporting Information), and the I-V measurements are only analyzed with the TVS method in this latter case. Figure 4 shows the statistical distribution of the ε_{0-SEL} and ε_{0-TVS} values obtained by fitting the SEL model and applying the TVS analysis on every I-V trace of the datasets (Fig. 2) for the $C6-PMo_{12}(0)$ and $C6-PMo_{12}(I)$ molecular junctions.
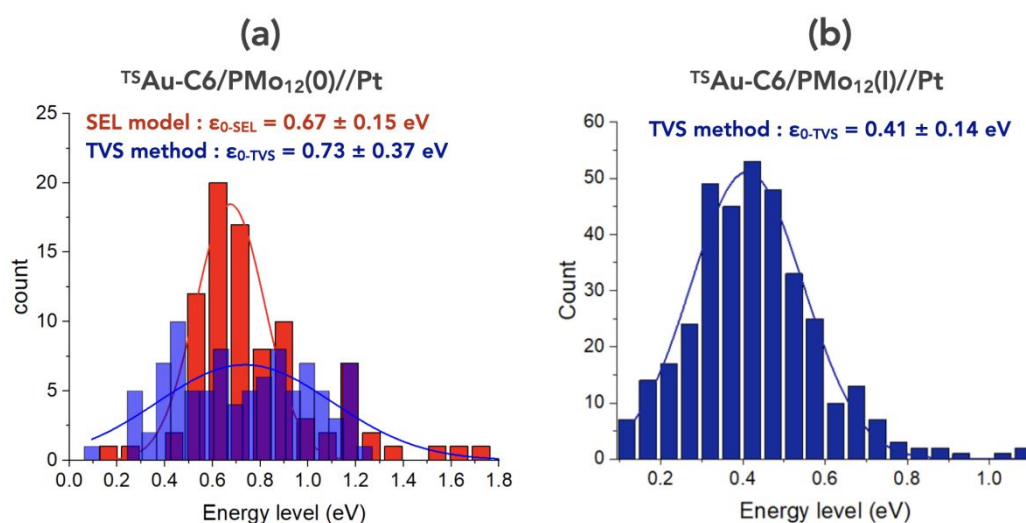
Nanoscale Accepted Manuscript

Figure 4. *Statistical distribution of the energy level (SEL model and TVS method) involved in the ET properties for (a) ^{TS}Au-C6/PMo$_{12}$(0)//Pt and (b) ^{TS}Au-C6/PMo$_{12}$(I)//Pt. The solid lines are the fits by a Gaussian distribution with the mean value ± standard deviation indicated in the panels.*

We conclude that the increase of the current for the ^{TS}Au-C6/PMo$_{12}$(I)//Pt molecular junction is mainly due to the fact that MO involved in the electron transport comes closer to the Fermi level of the electrodes. In the case of the SEL model applied on the dataset of the ^{TS}Au-C6/PMo$_{12}$(0)//Pt samples, the electrode coupling energies Γ_1 and Γ_2 are also broadly distributed (0.01 - 1 meV, Fig. S9). For the TVS method, the average values of Γ_{TVS} determined using Eq. (3) are given in Table 2 and are on reasonable agreement with the SEL values.

		^{TS}Au-C6/PMo$_{12}$(0)//Pt	^{TS}Au-C6/PMo$_{12}$(I)//Pt
TVS	$\varepsilon_{0\text{-TVS}}$ **(eV)**	0.73 ± 0.37	0.41 ± 0.14
	Γ_{TVS} **(meV)**	0.32	0.1
SEL	$\varepsilon_{0\text{-SEL}}$ **(eV)**	0.67 ± 0.15	n.a.
	Γ_1 **(meV)**	0.1-0.2	
	Γ_2 **(meV)**	0.1-0.2	

Table 2. *Parameters of the Gaussian fits of the molecular energy level ε_0 for the TVS method and the SEL model (Fig. 4) and of the electrode coupling energies. For the electronic coupling to the electrodes (Γ_1 and Γ_2) a range is indicated due to a large dispersion (see Fig. S9 in the Supporting Information).*

To gain a more detailed understanding and because the I-V traces, and consequently the values of the energy levels and electrode coupling energies, are largely dispersed (Figs. 2 and 4), we apply machine learning (ML) and clustering tool to classify the individual I-V trace according to common characteristic features appearing in the dataset (pattern recognition).[42-45] More specifically, we use an unsupervised, reference-free tool developed by some of us.[44, 45] Following the benchmark reported in Ref. 45, we use: (i) the UMAP(cos.) (uniform manifold approximation and projection with a cosine distance metric) for the construction of the feature space, (ii) the GAL (graph average linkage) for the clustering algorithm with an optimal number of 5 clusters[45] (more detail section 7 in the Supporting Information). Figure 5a shows the feature space obtained for the dataset of the C6-PMo$_{12}$(0) molecular junctions (note that for this ML-based analysis, the complete dataset of 600 I-Vs is used). Figure 5b shows the mean Ī-V of the 5 clusters. The same data are shown for C6-PMo$_{12}$(I) in Figs. 5c and 5d.
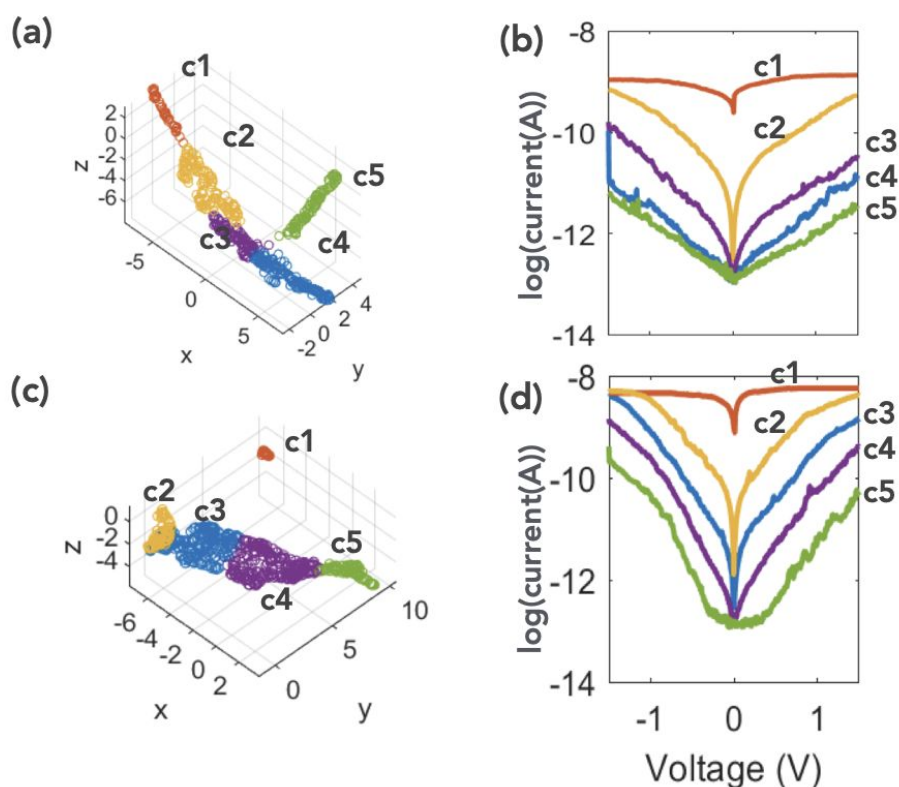
Figure 5. *(a) Feature space and (b) mean $\bar{I}$-V for each clusters c1 to c5 for the ^{TS}Au-C6-PMo$_{12}$(0)//Pt junctions. (c) Feature space and (d) mean $\bar{I}$-V for each clusters c1 to c5 for the ^{TS}Au-C6-PMo$_{12}$(I)//Pt junctions.*

For the ^{TS}Au-C6-PMo$_{12}$(0)//Pt junctions, cluster 1 corresponds to I-Vs (7.7% of the dataset) saturating during the measurements, the mean $\bar{I}$-V curve of clusters 2 to 5 shown in Fig. 5b were analyzed with the SEL models and the TVS approach (the complete datasets of I-Vs belonging to each cluster, the SEL fits and TVS curves are given in the Supporting Information (Figs. S14-S16). Cluster 2 (24.6%) and cluster 3 (18.8%) are characterized by the same ε_0 value (0.60-0.61 eV by TVS, 0.67-0.69 eV by SEL) with a higher electronic coupling to the electrodes for cluster 2 ($\Gamma_{TVS} \approx 0.63$ meV; $\Gamma_1 \approx 0.44$ meV and $\Gamma_2 \approx 0.37$ ^{m}eV by SEL) compared to cluster 3 ($\Gamma_{TVS} \approx 0.14$ meV; $\Gamma_1 \approx 0.11$ meV and $\Gamma_2 \approx 0.083$ meV by SEL), data summarized in Table 3. Cluster 4 (29.2%) and cluster 5 (19.7%), with the lowest current and almost

similar mean Ī-V traces (Fig. 5b) are, however, characterized by slightly different couple of the ε_0 and Γ_{TVS} parameters that counterbalance each other (larger ε_0 for cluster 5 with a better electrode coupling : $\varepsilon_{0-TVS} \approx 0.72$ eV, $\Gamma_{TVS} \approx 0.28$ meV for cluster 5 vs. $\varepsilon_{0-TVS} \approx 0.55$ eV, $\Gamma_{TVS} \approx 0.054$ meV for cluster 4 (Table 3) (same behavior for the data obtained by SEL, Table 3). A larger ε_0, i.e. a MO far away from the Fermi energy tends to decrease the current, while a better electrode coupling energy tends to increase the current. We also note that clusters 2, 4 and 5 display almost symmetric mean Ī-Vs (with $R^- = \bar{I}(-1.5 \text{ V})/(1.5 \text{ V}) < 2$), while a slight negative asymmetry is observed for cluster 3 with $R^- \approx 2.8$ (Table 3). This trend is confirmed by a statistical analysis on all the I-Vs belonging to each clusters (Fig. S7). For the ^{TS}Au-C6-PMo$_{12}$(I) devices, cluster 1 (2.8% of the I-V traces) concerns again saturating I-Vs, which are not analyzed. The mean Ī-V curves for the 4 other clusters are analyzed by the TVS method (Figs. S20). The clusters 2 and 3 are characterized by a ε_{0-TVS} value around 0.4 eV and Γ_{TVS} 0.35 - 1.1 meV (Table 3), while clusters 4 and 5 have a lower ε_{0-TVS} around 0.3 eV but also a lower Γ_{TVS} (0.068-0.094 meV). In the case of the reduced POM, we note that all the mean Ī-Vs traces are asymmetric with the clusters 4 and 5 displaying the highest R^- values (5-8, Table 3).

cluster	^{TS}Au-C6/PMo$_{12}$(0)//Pt				^{TS}Au-C6/PMo$_{12}$(I)//Pt			
	C2 (24.6%)	C3 (18.8%)	C4 (29.2%)	C5 (19.7%)	C2 (12.5%)	C3 (35.7%)	C4 (35.5%)	C5 (13.5%)
$\varepsilon_{0\text{-TVS}}$ (eV)	0.61	0.60	0.55	0.72	0.43	0.38	0.33	0.28
Γ_{TVS} (meV)	0.63	0.14	0.054	0.28	1.1	0.35	0.094	0.068
$\varepsilon_{0\text{-SEL}}$ (eV)	0.69	0.67	0.60	0.81	n.a.			
Γ_1 (meV)	0.44	0.11	0.038	0.046				
Γ_2 (meV)	0.37	0.083	0.036	0.032				
$(\Gamma_1 \cdot \Gamma_2)^{1/2}$	0.40	0.096	0.037	0.038				
R^-	≈1.7	≈2.8	≈1.1	≈1.5	≈2*	≈2.6	≈5	≈8

Table 3. *Parameters of the molecular energy level ε_0 for the TVS method and the SEL model of the mean $\bar{I}$-V curves belonging to the different clusters (Fig. 5) and of the electrode coupling energies (detailed data shown in Figs. S10-S15 in the Supporting Information). R^- is the asymmetry ratio, $R^- = \bar{I}(-1.5\ V)/\bar{I}(1.5\ V)$, calculated from the mean $\bar{I}$-Vs of each cluster. * stands for underestimated value since the current saturates below around -1V in that case.*

Discussion.

From the I-V analysis (both on the mean $\bar{I}$-V, Figs. 2 and 4, and the statistical measurements, Figs. S18 - S23) we propose the energy scheme shown in Fig. 6 for the ^{TS}Au-C6/PMo$_{12}$(0)//Pt and ^{TS}Au-C6/PMo$_{12}$(I)//Pt molecular junctions. For the PMo$_{12}$(0), the ET is mediated by the LUMO that is at about 0.7 eV above the Fermi

energy ($\varepsilon_{0\text{-SEL}}$= 0.67 ± 0.15 eV, $\varepsilon_{0\text{-TVS}}$ = 0.73 ± 0.37 eV, Table 2) as determined by the SEL and TVS analysis of the I-V measurements (Fig. 6a). This value is consistent with a LUMO at -4.5 eV (*vs.* vacuum energy, theory)[46] and work functions (WF) of Au (≈4.8-5.2 eV) and Pt (≈5.6 eV), the exact alignment of the MOs with the Fermi energy of the electrodes being dictated by the interface dipole and the details of the molecule/metal contact[47-49]. We note that this LUMO energy level is also consistent with the cyclic voltammetry measurements (LUMO at ~ -4.9 eV, see Fig. S3). According to previously reported calculations, the HOMO is located deeper (HOMO-LUMO gap of ca. 1.9-2.2 eV)[46, 50] and it is not involved in the ET property of the molecular junction. For the one-electron reduced $PMo_{12}(I)$, the added electron is localized on a SOMO located near to the electrode Fermi level as also reported when open-shell radicals are incorporated in molecular junctions.[51-56] Generally speaking, it is known from ab-initio calculations that the SOMO-SUMO gap of a series one-electron reduced POMs is low at around ~0.2 eV,[57] and thus both levels can now easily contribute to ET in the molecular junctions, leading to the experimentally observed enhanced conductance (Fig. 6b). Consequently, we ascribe the experimental value of $\varepsilon_{0\text{-TVS}}$ = 0.41 ± 0.14 eV (Table 2) to the SUMO level, while the SOMO remains close to the Fermi energy. This result pinpoints the good stability of the open-shell structure of the PMo(I) molecules when inserted in the junctions at room temperature, while previous attempts to incorporate organic radicals in molecular junctions showed a stable open-shell junction only at low temperature and/or under UHV.[55, 58, 59] This is likely because the SOMO is localized on the Mo and therefore it is embedded inside the molecule and partly protected from a too strong interaction with the metal electrodes in a similar way as recently demonstrated for a verdazyl radical, stable in its open-shell configuration at room temperature in molecular junctions.[56]

We note that I-V measurements on a reference sample without the POMs, i.e. ^{TS}AU-C6//Pt junctions, give a higher value $\varepsilon_0 \approx 0.9$ eV (section 8 in the Supporting Information), in good agreement with previous results for the LUMO of alkyl chains on Au.[60, 61] Thus the above determined values of ε_0 can be solely attributed to MOs of the POMs, the alkyl chain SAM playing the role of a thin tunnel barrier between the Au electrode and the POMs (in addition to a template structure to the electrostatic deposition of the POMs).

The difference between the ET through $PMo_{12}(0)$ and $PMo_{12}(I)$ is the shape of the I-Vs: almost symmetric for $PMo_{12}(0)$ and asymmetric for $PMo_{12}(I)$. Considering the energy diagram for the ^{TS}Au-C6/$PMo_{12}(0)$//Pt (Fig. 6a), the position of the LUMO near the grounded Pt C-AFM tip is likely to induce a slight negative asymmetry (*i.e.*, more current at negative voltages applied on the Au substrate when the Fermi energy of the Au electrode moves upper towards the LUMO level) and allows LUMO-assisted ET (blue arrow in Fig. 6a), while for V>0 the LUMO does not enter in the energy window defined by the Fermi energy of the two electrodes, Fig. 6a.[62-65] However, the difference in the work function (WF) of the electrodes (lower WF for Au than for Pt) can induce a reverse behavior, a positive asymmetry, *i.e.*, more direct tunneling current (green arrow in Fig. 6a) for a positive voltage applied on the electrode with the lowest WF (i.e. Au),[66] as observed on the I-V curves of the C6 SAMs (Fig. S24 in the supporting information) showing a slight positive asymmetry. Since the ^{TS}Au-C6/$PMo_{12}(0)$//Pt and the ^{TS}Au-C6//Pt junctions display current levels of the same order of magnitude (Fig. 2 and Fig. S24 in the Supporting Information), these two effects of opposite behavior can counterbalance each other, leading to the observed almost symmetric I-V behavior.

On the contrary, all the I-Vs of the dataset for the ^{TS}Au-C6/PMo$_{12}$(I)//Pt sample, display a negative asymmetry (Fig. S21). Since the SOMO of the open-shell POM is lying close to the Fermi energy of the electrodes and the SOMO-SUMO gap is small (≈ 0.4 eV), we hypothesize that at V<0 the two levels can be involved in the ET of the POM junction (Fig. 6b), while only the SOMO is considered at V>0 since it remains close to the Fermi energy and the SUMO is no longer contributing to the ET. We assume that the direct tunneling is negligible since the PMo$_{12}$(I) junctions have a current one decade higher than the C6 alone SAMs. Thus, the fact that two channels contribute to the ET at V<0 might explain this negative asymmetry. These simple hypothesis must be confirmed by more detailed *ab-inito* calculations, the exact I-V behavior of the molecular junctions being dependent on the shift of MO under the applied bias (Stark effect), and, moreover, the presence of many dipoles in the molecular junctions (*e.g.,* between (PMo$_{12}$)$^{4-}$ and NH$_3^+$, (PMo$_{12}$)$^{4-}$ and TBA$^+$, charge transfer at the electrodes) is likely to change the energy landscape in the junction[67] and consequently the ET properties, especially the direction of the asymmetry of the I-Vs.[68-70] Finally, we note that change of the shape of the I-V curves (asymmetric vs. symmetric) has also been recently observed when switching a molecule between open-shell (radical) and closed-shell configurations.[54, 56]

It is also likely that the details on how these dipoles are organized (ordered vs. disordered), where they are located in the SAM, as well as the molecular ordering of the POMs influence the large dispersion of the I-V measurements observed here. This feature calls for more experiments, *e.g.* UHV-STM measurements with a molecular resolution, and AC-STM[71] allowing dielectric spectroscopy at the molecular level,[72] which are out of the scope of this work.

As noted the electrical neutrality in the SAM is ensured by a mixture of TBA^+ and NH_3^+ ions, which can also influence the ET in the molecular junction. It has been calculated that the presence of the positive counterions lowers the energy of the LUMO of the POMs. However the exact chemical nature of these ions has a negligible effect on this energy position.[73] Thus the TBA^+/NH_3^+ ratio (see Supporting Information) is not a crucial parameter. However, it was shown by the same authors that the presence of the counterions does not create additional conduction channels in the molecular junctions, but rather that they modify the potential landscape viewed by the POMs that transmit the electrons through the molecular junctions, and consequently can influence the I-V behavior. Thus, we surmise that a part of the large dispersion of the I-V curves might be due to local variations of this TBA^+/NH_3^+ ratio and how these counterions are organized (*vide supra*).
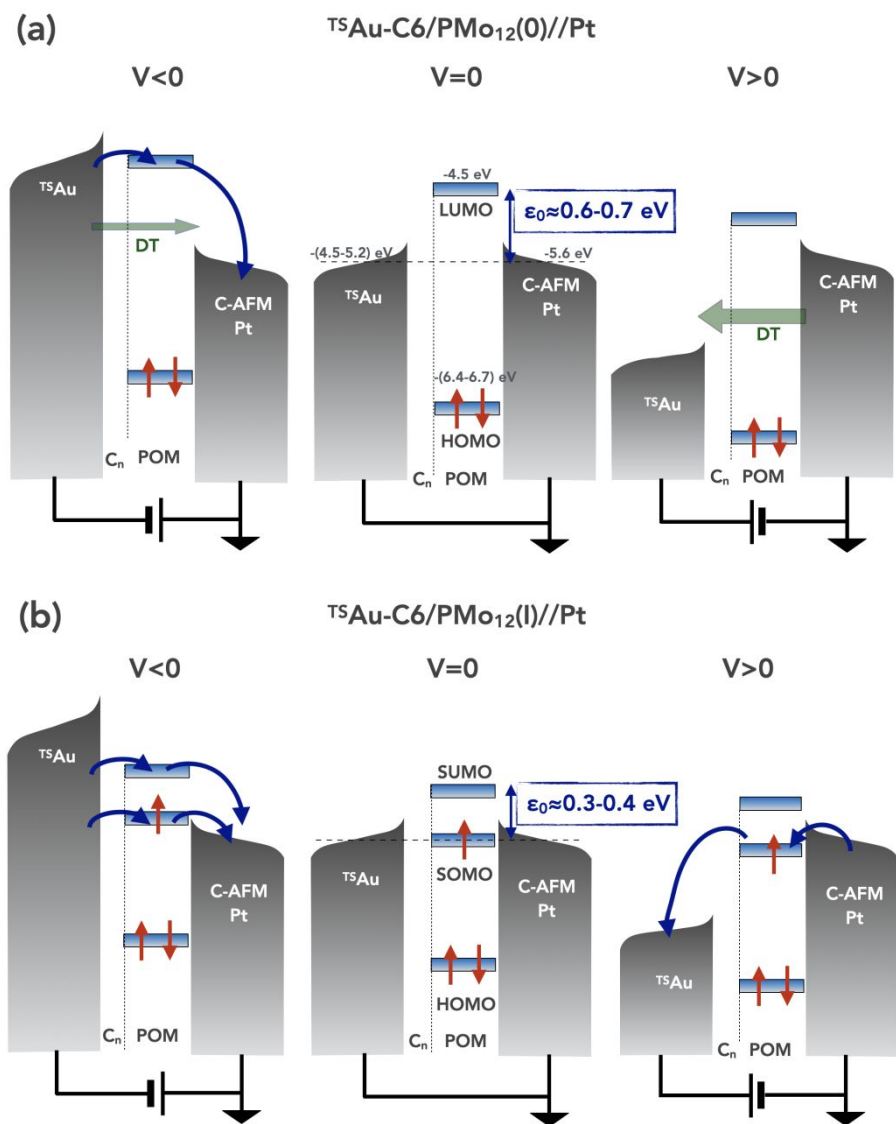
Figure 6. Hypothesized schemes of the energy diagrams : (a) ^{TS}Au-C6/PMo$_{12}$(0)//Pt and (b) ^{TS}Au-C6/PMo$_{12}$(I)//Pt junctions at a negative, null and positive bias applied on the ^{TS}Au substrate (the C-AFM tip grounded). The blue arrows indicate the MO-mediated electron transport and the green arrows show the direct tunneling (the wider the arrow, the larger the tunneling current). The MO energies (vs. vacuum energy) are given as reported from calculations (see text) and the ε_0 values are taken from our experiments (Figs. 2 and 4, Table 2).

The ML and clustering methods allow us to refine the analysis of the large dispersion of the I-V dataset. For the ^{TS}Au-C6/PMo$_{12}$(0)//Pt, the two clusters with the highest current level (#2 and #3, 0.1 - 1 nA at +/- 1.5V, Fig. 5b) have the same LUMO energy ($\approx$ 0.6 eV) in agreement with the average value deduced from statistics on the full dataset (Fig. 4). They only differ by the electronic coupling to the electrodes (a factor about 4.5), which likely reflects fluctuations of the C-AFM tip contact on the SAM. The two other clusters at low current (#4 and #5, $\approx$ 10 pA at +/- 1.5 V, Fig. 5b) have more dispersed values of the LUMO but they likely include noisy I-V traces near the sensitivity limit of the current-voltage preamplifier (Fig. S16). We note, however, that the cluster 3 displays an asymmetric shape of the I-V in contrast to the I-Vs of the other clusters and the global mean Ī-V (Fig. 2, Fig. S16, Table 3). For the ^{TS}Au-C6/PMo$_{12}$(I)//Pt, we can distinguish two series of two clusters each. In the first series, the clusters 2 and 3 with the highest current level ($\approx$ 10 nA at +/- 1.5 V, Fig. 5d) are characterized by a MO level at 0.38-0.43 eV with the largest electronic coupling to the electrodes (0.35-1.1 meV), and, in the second series, the clusters 4 and 5 show a slightly lower energy level ($\approx$ 0.3 eV), but a worse electrode coupling (0.07-0.1 meV) leading to the lowest current level ($\approx$ 10-100 pA et +/- 1.5 V, Fig. 5d). This feature may be due to different configurations of the PMo$_{12}$(I) between the C6 SAM and the C-AFM tip, as well as, fluctuations of the C-AFM tip contact (not easily distinguishable at this experimental level). The main difference compared to the PMo$_{12}$(0) case is that all the clusters (Fig. S21) display asymmetric I-Vs (as for the global mean Ī-V in Fig. 2) with the largest asymmetry for clusters 4 and 5. Thus this asymmetric feature in these ^{TS}Au-C6/PMo$_{12}$//Pt junctions can be viewed as a finger print of the reduced PMo$_{12}$(I) and the asymmetric cluster 3 for the PMo$_{12}$(0) device could be ascribed to the presence of a small fraction of reduced Mo in that case as observed from XPS (see Fig. S5 in the SI).

Conclusion.

We investigated the electronic properties of switchable redox polyoxometalates (phosphomolybdate, PMo_{12}) by a combination of i) electron transport measurements at the nanoscale (C-AFM on self-assembled monolayers), ii) analytical models statistically applied on large current-voltage datasets and iii) unsupervised machine learning and clustering algorithms. The main results are summarized as follows:

1. We demonstrate a reversible redox switching triggered *in situ* by UV photoreduction.

2. The one-electron reduced PMo_{12} (open-shell state) is stable in the molecular junctions in air and at room temperature, the spontaneous return to its oxidized state laps for several hours to days.

3. The reduced PMo_{12} molecular junctions are characterized by an increase of the conductance (a factor ∼ 10) and asymmetric current-voltage curves.

4. The electron transport in the pristine PMo_{12} junctions is controlled by the LUMO located at ∼ 0.6-0.7 eV above the Fermi energy of the electrodes, with 25% of the junction dataset characterized by a better electronic coupling to the electrodes.

5. The electron transport in the reduced PMo_{12} junctions and the asymmetric current-voltage behavior is ascribed to a combined electron transmission through energetically closed (0.3-0.4 eV) SOMO and SUMO levels near resonance with the Fermi energy of the electrodes. This latter point calls for detailed theoretical studies.

Materials and methods

Synthesis and sample fabrication.

Molecule synthesis. The $PMo_{12}(0)$ and $PMo_{12}(I)$ were prepared as previously reported by some of us,[16] and the characterizations (^{31}P NMR, cyclic voltammetry, solution UV-vis spectroscopy, XPS spectra on powder) are given in the Supporting Information (section 1).

Bottom metal electrode fabrication. Template stripped gold (^{TS}Au) substrates were prepared according to the method previously reported.[17, 74, 75] In brief, a 300–500 nm thick Au film is evaporated on a very flat silicon wafer covered by its native SiO_2 and then transferred to a glued clean glass piece which is mechanically stripped with the Au film attached on the glass piece, letting exposed a very flat (RMS roughness of 0.4 nm, the same as the starting SiO_2 surface used as the template).

Self-assembled monolayers. The SAMs on ^{TS}Au were fabricated following a protocol developed and optimized in a previous work for the electrostatic immobilization of POMs on amine-terminated SAMs.[11] In brief, we first dipped the freshly prepared metal substrate in a solution of 6-aminohexane-1-thiol hydrochloride ($HS-(CH_2)_6-NH_2$) at a concentration of 10^{-3} M in ethanol overnight in the dark (see details in section 2 in the Supporting Information). Then the samples were dipped in a solution of POMs at a concentration of 10^{-3} M in acetonitrile for several hours (we checked that the thickness of the POM layer was independent of the immersion time when > 1h).

Spectroscopic ellipsometry.

The thickness of the SAMs was measured by spectroscopic ellipsometry (UVISEL ellipsometer (HORIBA), section 3 in the Supporting Information).

C-AFM in ambient conditions. We measured the electron transport properties at the nanoscale by C-AFM (ICON, Bruker) at room temperature using a tip probe in platinum (with loading force of ca. 6-8 nN). The voltage was applied on the substrate, the tip is grounded via the input of the current-voltage preamplifier. We used a "blind" mode to measure the current-voltage (I-V) curves and the current histograms: a square grid of 10×10 points was defined with a pitch of 50 to 100 nm. At each point, the I-V curve (back and forth) is acquired leading to the measurements of 200 traces per grid. This process was repeated 3 times at different places (randomly chosen) on the sample, and up to 600 I-V traces were used to construct the current-voltage histograms (section 4 in the Supporting Information).

Photoreduction.

A UV lamp (Analytik Jena) was used for the UV light irradiation at 302 nm for the CAFM measurements (section 5 in the Supporting Information).

Associated content

The Supporting Information is available free of charge at xxxxxx.

- Details on synthesis, RMN, cyclic voltammetry, UV-vis spectroscopy, XPS, fabrication of electrodes and self-assembled monolayers, ellipsometry, C-AFM data analysis and fit protocols, UV illumination setup, I-V curves of the redox cycles, machine learning and clustering details on the validation and analysis of the different clusters of I-V traces, data for reference samples (without POMs).

Author Contributions

C.H. and D.G. fabricated the SAMs and performed the physicochemical characterizations (UV-vis, XPS), F.V. and A.P. synthesized and characterized the POMs. C.H. did all the CAFM measurements, C.H. and D.V. analyzed the data. The machine learning analysis was conducted in the framework of a collaboration with

M.C., C.H. under the supervision of M.L.P. performed the machine learning analysis. A.P. and D.V. conceived and supervised the project. This work is part of the PhD thesis of C.H., S.L. and D.V. supervised the thesis. The manuscript was written by D.V. with the contributions of all the authors. All authors have given approval of the final version of the manuscript.

Note

The authors declare no competing financial interest.

References.

1.   M. J. Turo, L. Chen, C. E. Moore and A. M. Schimpf, *J Am Chem Soc*, 2019, **141**, 4553-4557.

2.   C. Busche, L. Vila-Nadal, J. Yan, H. N. Miras, D. L. Long, V. P. Georgiev, A. Asenov, R. H. Pedersen, N. Gadegaard, M. M. Mirza, D. J. Paul, J. M. Poblet and L. Cronin, *Nature*, 2014, **515**, 545-549.

3.   A. Balliou, A. M. Douvas, P. Normand, D. Tsikritzis, S. Kennou, P. Argitis and N. Glezos, *J. Appl. Phys.*, 2014, **116**, 143703.

4.   A. Balliou, G. Papadimitropoulos, G. Skoulatakis, S. Kennou, D. Davazoglou, S. Gardelis and N. Glezos, *ACS Appl. Mater. Interfaces*, 2016, **8**, 7212-7220.

5.   X. Chen, J. Pan, J. Fu, X. Zhu, C. Zhang, L. Zhou, Y. Wang, Z. Lv, Y. Zhou and S.-T. Han, *Adv. Electron. Mater.*, 2018, **4**, 1800444.

6.   X. Chen, P. Huang, X. Zhu, S. Zhuang, H. Zhu, J. Fu, A. S. Nissimagoudar, W. Li, X. Zhang, L. Zhou, Y. Wang, Z. Lv, Y. Zhou and S.-T. Han, *Nanoscale Horiz.*, 2019, **4**, 697-704.

7.   A. M. Douvas, E. Makarona, N. Glezos, P. Argitis, J. A. Mielczarski and E. Mielczarski, *ACS Nano*, 2008, **2**, 733-742.

8.   X. Yi, N. V. Izarova, M. Stuckart, D. Guerin, L. Thomas, S. Lenfant, D. Vuillaume, J. van Leusen, T. Duchoň, S. Nemšák, S. D. M. Bourone, S. Schmitz and P. Kögerler, *J Am Chem Soc*, 2017, **139**, 14501-14510.

9.   A. Balliou, M. Bouroushian, A. M. Douvas, G. Skoulatakis, S. Kennou and N. Glezos, *Nanotechnology*, 2018, **29**, 275204.

10.   M. Laurans, K. Dalla Francesca, F. Volatron, G. Izzet, D. Guerin, D. Vuillaume, S. Lenfant and A. Proust, *Nanoscale*, 2018, **10**, 17156-17165.

11.   K. Dalla Francesca, S. Lenfant, M. Laurans, F. Volatron, G. Izzet, V. Humblot, C. Methivier, D. Guerin, A. Proust and D. Vuillaume, *Nanoscale*, 2019, **11**, 1863-1878.

12.   M. Laurans, K. Trinh, K. Dalla Francesca, G. Izzet, S. Alves, E. Derat, V. Humblot, O. Pluchery, D. Vuillaume, S. Lenfant, F. Volatron and A. Proust, *ACS Appl. Mater. Interfaces*, 2020, **12**, 48109-48123.

13.   O. Linnenberg, M. Moors, A. Notario-Estevez, X. Lopez, C. de Graaf, S. Peter, C. Baeumer, R. Waser and K. Y. Monakhov, *J Am Chem Soc*, 2018, **140**, 16635-16640.

14.   A. Notario-Estevez, X. Lopez and C. de Graaf, *Dalton Trans*, 2021, **50**, 5540-5551.

15.   C. Rocchiccioli-Deltcheff, M. Fournier, R. Franck and R. Thouvenot, *Inorganic Chemistry*, 1983, **22**, 207-216.

16.   V. Artero and A. Proust, European Journal of Inorganic Chemistry, 2000, **2000**, 2393-2400.

17.   E. A. Weiss, G. K. Kaufman, J. K. Kriebel, Z. Li, R. Schalek and G. M. Whitesides, *Langmuir*, 2007, **23**, 9686-9694.

18.   G. M. Whitesides, H. A. Biebuyck, J. P. Folkers and K. L. Prime, *Journal of Adhesion Science and Technology*, 1991, **5**, 57-69.

19.   D. V. Vezenov, A. Noy, L. F. Rozsnyai and C. M. Lieber, *Journal of the American Chemical Society*, 1997, **119**, 2006-2015.

20.   N. Katsuhiko, K. Atsushi, U. Akihiro and T. Isao, *Chemistry Letters*, 2002, **31**, 80-81.

21.   W. A. Marmisolle, D. A. Capdevila, E. de la Llave, F. J. Williams and D. H. Murgida, *Langmuir*, 2013, **29**, 5351-5359.

22.   D. G. Kurth, D. Volkmer, M. Ruttorf, B. Richter and A. Müller, *Chemistry of Materials*, 2000, **12**, 2829-2831.

23.   T. Yamase, Chemical Reviews, 1998, **98**, 307-326.

24.   S. Datta, Electronic transport in mesoscopic systems, Cambridge University Press, 1995.

25.   J. C. Cuevas and E. Scheer, Molecular Electronics: An introduction to theory and experiment, World Scientific, 2010.

26.   M. Magoga and C. Joachim, *Phys. Rev. B*, 1999, **59**, 16011-16021.

27.   M. G. Reuter, M. C. Hersam, T. Seideman and M. A. Ratner, *Nano Letters*, 2012, **12**, 2243-2248.

28.   J. Trasobares, J. Rech, T. Jonckheere, T. Martin, O. Aleveque, E. Levillain, V. Diez-Cabanes, Y. Olivier, J. Cornil, J. P. Nys, R. Sivakumarasamy, K. Smaali, P. Leclere, A. Fujiwara, D. Theron, D. Vuillaume and N. Clement, *Nano Letters*, 2017, **17**, 3215–3224.

29.   X. D. Cui, A. Primak, X. Zarate, J. Tomfohr, O. F. Sankey, A. L. Moore, T. A. Moore, D. Gust, G. Harris and S. M. Lindsay, *Science*, 2001, **294**, 571-574.

30.   X. D. Cui, X. Zarate, J. Tomfohr, O. F. Sankey, A. Primak, A. L. Moore, T. A. Moore, D. Gust, G. Harris and S. M. Lindsay, *Nanotechnology*, 2002, **13**, 5-14.

Nanoscale Accepted Manuscript

31.   V. B. Engelkes and C. Daniel Frisbie, *The Journal of Physical Chemistry B*, 2006, **110**, 10011-10020.

32.   T. Morita and S. Lindsay, *J Am Chem Soc*, 2007, **129**, 7262-7263.

33.   K. Smaali, S. Desbief, G. Foti, T. Frederiksen, D. Sanchez-Portal, A. Arnau, J. P. Nys, P. Leclere, D. Vuillaume and N. Clement, *Nanoscale*, 2015, **7**, 1809-1819.

34.   J. M. Beebe, B. Kim, J. W. Gadzuk, C. D. Frisbie and J. G. Kushmerick, *PHYSICAL REVIEW LETTERS*, 2006, **97**, 026801.

35.   J. M. Beebe, B. Kim, C. D. Frisbie and J. G. Kushmerick, *ACS Nano*, 2008, **2**, 827-832.

36.   I. Bâldea, Physical Review B, 2012, **85**, 035442.

37.   E. H. Huisman, C. M. Guédon, B. J. van Wees and S. J. van der Molen, *Nano Lett*, 2009, **9**, 3909-3913.

38.   F. Mirjani, J. M. Thijssen and S. J. van der Molen, *Physical Review B*, 2011, **84**, 115402.

39.   I. Bâldea, Physical Chemistry Chemical Physics, 2015, **17**, 20217-20230.

40.   I. Bâldea, *Nanoscale*, 2013, **5**, 9222-9230.

41.   Z. Xie, I. Bâldea and C. D. Frisbie, *J Am Chem Soc*, 2019, **141**, 18182-18192.

42.   M. Lemmer, M. S. Inkpen, K. Kornysheva, N. J. Long and T. Albrecht, *Nature Communications*, 2016, **7**, 12922.

43.   J. M. Hamill, X. T. Zhao, G. Mészáros, M. R. Bryce and M. Arenz, *Physical Review Letters*, 2018, **120**, 016601.

44.   D. Cabosart, M. El Abbassi, D. Stefani, R. Frisenda, M. Calame, H. S. J. Van Der Zant and M. L. Perrin, *Appl. Phys. Lett.*, 2019, **114**, 143102.

45.   M. El Abbassi, J. Overbeck, O. Braun, M. Calame, H. S. J. van der Zant and M. L. Perrin, *Communications Physics*, 2021, **4**.

46.   R. Karcz, P. Niemiec, K. Pamin, J. Połtowicz, J. Kryściak-Czerwenka, B. D. Napruszewska, A. Michalik-Zym, M. Witko, R. Tokarz-Sobieraj and E. M. Serwicka, *Applied Catalysis A: General*, 2017, **542**, 317-326.

47.   D. Cornil, PhD thesis PhD, Univ. Mons, 2010.

48.   D. Cornil, H. Li, C. Wood, G. Pourtois, J.-L. Brédas and J. Cornil, *ChemPhysChem*, 2013, **14**, 2939-2946.

49.   N. Crivillers, S. Osella, C. Van Dyck, G. M. Lazzerini, D. Cornil, A. Liscio, F. Di Stasio, S. Mian, O. Fenwick, F. Reinders, M. Neuburger, E. Treossi, M. Mayor, V. Palermo, F. Cacialli, J. Cornil and P. Samorì, *Adv. Mater.*, 2013, **25**, 432-436.

50.   J. M. Maestre, X. Lopez, C. Bo, J.-M. Poblet and N. Casañ-Pastor, *Journal of the American Chemical Society*, 2001, **123**, 3749-3758.

51.   N. Crivillers, C. Munuera, M. Mas-Torrent, C. Simão, S. T. Bromley, C. Ocal, C. Rovira and J. Veciana, *Advanced Materials*, 2009, **21**, 1177-1181.

52.   G. Heimel, E. Zojer, L. Romaner, J. L. Brédas and F. Stellacci, *Nano Lett.*, 2009, **9**, 2559-2564.

53.   L. Yuan, C. Franco, N. Crivillers, M. Mas-Torrent, L. Cao, C. S. Suchand Sangeeth, C. Rovira, J. Veciana and C. A. Nijhuis, *Nature Communications*, 2016, **7**, 12066.

54.   M. Souto, L. Yuan, D. C. Morales, L. Jiang, I. Ratera, C. A. Nijhuis and J. Veciana, *J Am Chem Soc*, 2017, **139**, 4262-4265.

55.   J. Z. Low, G. Kladnik, L. L. Patera, S. Sokolov, G. Lovat, E. Kumarasamy, J. Repp, L. M. Campos, D. Cvetko, A. Morgante and L. Venkataraman, *Nano Lett*, 2019, **19**, 2543-2548.

56.   S. Naghibi, S. Sangtarash, V. J. Kumar, J. Z. Wu, M. M. Judd, X. Qiao, E. Gorenskaia, S. J. Higgins, N. Cox, R. J. Nichols, H. Sadeghi, P. J. Low and A. Vezzoli, *Angew Chem Int Ed Engl*, 2022, **61**, e202116985.

57.   L. Vila-Nadal, K. Peuntinger, C. Busche, J. Yan, D. Luders, D. L. Long, J. M. Poblet, D. M. Guldi and L. Cronin, *Angew Chem Int Ed Engl*, 2013, **52**, 9695-9699.

58.   R. Frisenda, R. Gaudenzi, C. Franco, M. Mas-Torrent, C. Rovira, J. Veciana, I. Alcon, S. T. Bromley, E. Burzuri and H. S. van der Zant, *Nano Lett*, 2015, **15**, 3109-3114.

59. R. Hayakawa, M. A. Karimi, J. Wolf, T. Huhn, M. S. Zollner, C. Herrmann and E. Scheer, *Nano Lett*, 2016, **16**, 4960-4967.

60. Y. Qi, O. Yaffe, E. Tirosh, A. Vilan, D. Cahen and A. Kahn, *Chemical Physics Letters*, 2011, **511**, 344-347.

61. G. Ricoeur, S. Lenfant, D. Guerin and D. Vuillaume, *Journal of Physical Chemistry C*, 2012, **116**, 20722-20730.

62. S. Lenfant, C. Krzeminski, C. Delerue, G. Allan and D. Vuillaume, *Nano Lett*, 2003, **3**, 741-746.

63. C. A. Nijhuis, W. F. Reus and G. M. Whitesides, *J Am Chem Soc*, 2009, **131**, 17814-17827.

64. X. Chen, M. Roemer, L. Yuan, W. Du, D. Thompson, E. del Barco and C. A. Nijhuis, *Nature Nanotech*, 2017, **12**, 797-803.

65. A. Vilan, D. Aswal and D. Cahen, *Chem Rev*, 2017, **117**, 4248-4286.

66. J. G. Simmons, *J. Appl. Phys.*, 1963, **34**, 2581-2590.

67. C. Van Dyck and A. J. Bergren, *Adv. Electron. Mater.*, 2018, **4**, 1700656.

68. W.-Y. Lo, N. Zhang, Z. Cai, L. Li and L. Yu, *Accounts of Chemical Research*, 2016, **49**, 1852-1863.

69. M. Baghbanzadeh, L. Belding, L. Yuan, J. Park, M. H. Al-Sayah, C. M. Bowers and G. M. Whitesides, *J Am Chem Soc*, 2019, **141**, 8969-8980.

70. Y. Han, M. S. Maglione, V. Diez Cabanes, J. Casado-Montenegro, X. Yu, S. K. Karuppannan, Z. Zhang, N. Crivillers, M. Mas-Torrent, C. Rovira, J. Cornil, J. Veciana and C. A. Nijhuis, *ACS Appl. Mater. Interfaces*, 2020, **12**, 55044-55055.

71. S. J. Stranick and P. S. Weiss, *The Journal of Physical Chemistry*, 1994, **98**, 1762-1764.

72. V. Stetsovych, S. Feigl, R. Vranik, B. Wit, E. Rauls, J. Nejedly, M. Samal, I. Stary and S. Mullegger, *Sci Rep*, 2022, **12**, 2865.

73. P. Lapham, L. Vila-Nadal, L. Cronin and V. P. Georgiev, *J Phys Chem C*, 2021, **125**, 3599-3610.

74. M. Hegner, P. Wagner and G. Semenza, *Surf. Sci.*, 1993, **291**, 39-46.

75. E. Weiss, R. Chiechi, G. Kaufman, J. Kriebel, Z. Li, M. Duati, M. Rampi and

G. Whitesides, *J. Am. Chem. Soc*, 2007, **129**, 4336-4349.

Nanoscale Accepted Manuscript